Supplementary Material for "Remotely induced magnetism in a normal metal using a superconducting spin-valve" by M.G. Flokstra et al.

This *Supplementary Material* contains additional discussion on the growth and characterisation of the samples, on the low energy muon spin rotation measurement technique and data analysis and on the suggested mechanism of spin triplet spin currents to explain the main findings of the manuscript. While not essential to the understanding or conclusions of the manuscript, specialist readers may find the additional material useful and informative.

1 Sample Design and Preparation

1.1 Sample design

The basis for the NSFnF architecture used in this work are conventional bottom-pinned exchange biased thin-film spin-valve structures, capped with a superconductor (S) / normal metal (N) bilayer. The generic spin-valve structure is antiferromagnet (AF) / pinned ferromagnet (F) / normal metal spacer (n) / free ferromagnet (F) / cap layer, where exchange bias between the antiferromagnet and pinned ferromagnet gives a unidirectional anisotropy to the pinned ferromagnet, whilst the free ferromagnetic layer lacks this strong anisotropy and is decoupled from the pinned layer by the spacer. The ferromagnetic layers are Co due its comparatively long spin diffusion length. The full sample stack for the base structure is thus, Au(70) / Nb(50) / Co(2.4) / Nb(3) / Co(1.2) / IrMn(4) / Co(3) / Ta(7.5) / Si-substrate with numbers in brackets indicating the thicknesses of the corresponding layers in nm. In order for the antiferromagnetic IrMn layer to exchange bias the thin (1.2 nm) Co pinned layer, it was necessary to deposit the IrMn on a magnetically saturated ferromagnetic interface or, alternatively, for the whole sample stack to be annealed above the Néel temperature of the IrMn in a saturating magnetic field. Since this latter process could potentially cause inter-diffusion of the layers at the critical interfaces, the former approach was used and so below the antiferromagnetic IrMn layer we first deposited a 3 nm Co buffer layer. During the deposition a homogenous magnetic field is applied in the plane of the samples and this ensures that the lowest buffer Co layer is saturated. The lowest Ta layer acts as a buffer to provide a textured surface to promote the growth of the subsequent

magnetic layers. The final 70 nm Au layers has a dual purpose. It serves as a cap to prevent oxidation of the stack after growth and as a layer to probe with muons to look for induced magnetism. The saturation field of the free Co layer is about 1-5 mT which is well below the typical applied field of 10-15 mT during the muon experiments. Magnetization measurements on the base structure at T = 10 K are presented in Fig.1 which shows the switching of the three Co layers. The free Co (2.4 nm) layer clearly is unbiased and switches sharply with a switching field less than 5 mT. The pinning of the buffer Co (3 nm) layer shows an exchange bias of about 45 mT while the pinning of the thinner Co (1.2 nm) shows a bias of about 200 mT.

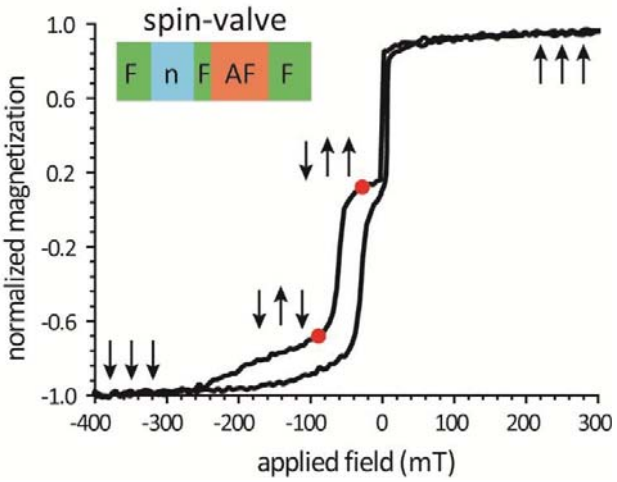

Fig.1. VSM magnetisation data on the NSFnF architecture at a temperature of 10 K and field applied along the exchange bias direction. Indicated with arrows are the magnetization orientations of the F layers.

Two variants of the base structure were used as well. One variant has a much thinner Au cap of 5 nm allowing the Nb layer to be probed without mixing in a high contribution from muons stopping in the Au layer, and one variant where the IrMn(4)/Co(3) is absent such that in an applied field of about 150 G both F layers are saturated and perfectly aligned.

1.2 Sample preparation

Samples were prepared by dc magnetron sputtering on Si (100) substrates in a system with a base pressure of 10^{-8} mbar. During growth substrates were at ambient temperature and growth was carried

out in a single vacuum cycle at a typical Ar flow of 24 sccm and pressure of 2-3 μbar and a substrate-sample distance of approximately 25 mm, with a typical growth rate of 0.2 nms^{-1}. Growth rates for each material were calibrated using fits to the Kiessig fringes in low angle X-ray reflectivity measurements of single layers of each material. The superconducting critical temperature of Nb is strongly dependent on vacuum conditions and is also thickness dependent for films less than 50 nm thick. Separate single films of Nb were grown in the same vacuum cycle as the samples and typically had a critical temperature of $T_c \sim 8.5$ K for a 50 nm film.

1.2.1 X-ray reflectometry

X-ray reflectometry (XRR) measurements were made on a series of samples with varying layer thicknesses. The data were collected on a Rigaku™ rotating anode SmartLab x-ray diffractometer using Cu $K\alpha_1$ radiation and analysed using the GenX software[*J. Appl. Cryst.* **40**, 1174 (2007)]. The data presented here are for a nominal sample structure of Si / Ta(75) / Co(30) / IrMn(40) / Co(12) / Nb(30) / Co(24) / Nb(400) / Au(700) with numbers in brackets indicating the thicknesses of the corresponding layers in nm. The XRR and model from this representative sample are shown in Fig.2. The extracted parameters are shown in Table 1. As can be seen there is good agreement with the nominal structure. The interfacial roughness is small for all layers. Of particular note for this work is the low interfacial roughness between the top Au layer and the adjacent thick Nb layer.

Table 1. X-ray reflectometry fitting parameters. The error in the extracted values is difficult to robustly quantify and a basic analysis of their effect on the figure of merit returned by the fit indicated them to be of order 10%. The fits are dominated by interfaces with a large change in scattering length density (Si/Ta, Ta/Co, Nb/Au and Au/air).

Layer	Density (f.u./ Å^3)	Thickness (Å)	Interfacial Roughness (Å)
Au	0.058	783	14
Nb	0.055	404	7
Co	0.09	22	4
Nb	0.055	34	5
Co	0.09	12	3
IrMn	0.025	45	3

Co	0.09	27	4
Ta	0.055	81	5
SiO_x	0.041	36	4
Si substrate	0.0497	∞	1

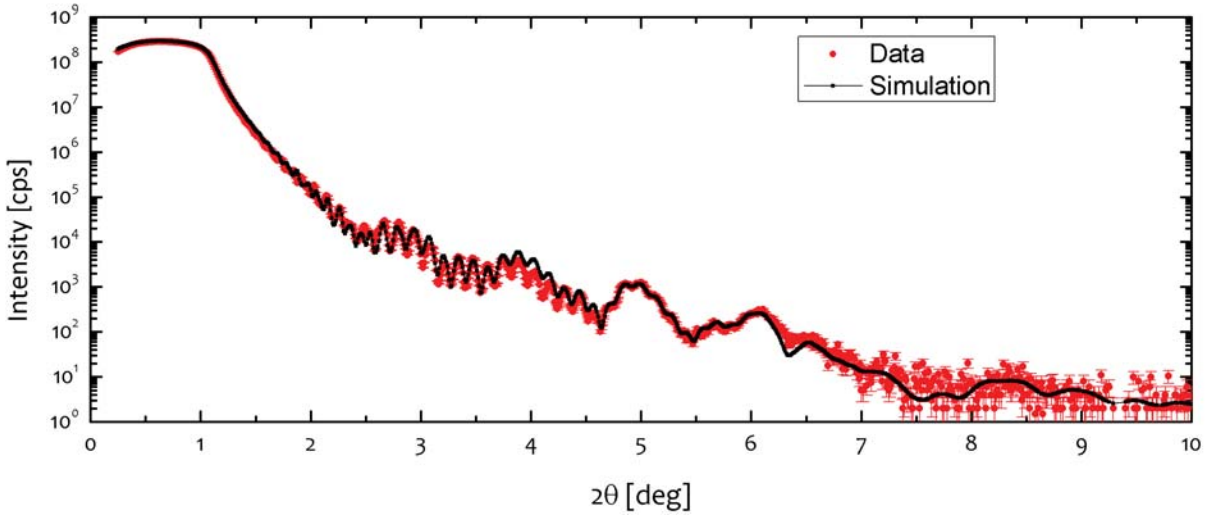

Fig.2. The XRR data and fit for the sample described in the text.

1.2.2 Atomic force microscopy

Atomic force microscopy images of the Au surface of the samples were acquired on a Veeco Dimension 3100 system in tapping mode with a standard (non-magnetic tip). Images were acquired at various regions of the sample and a representative image is shown in Fig.3. Averaging over five $2\times2\mu m^2$ regions provided a root mean square roughness (RMS) of 7±1Å.

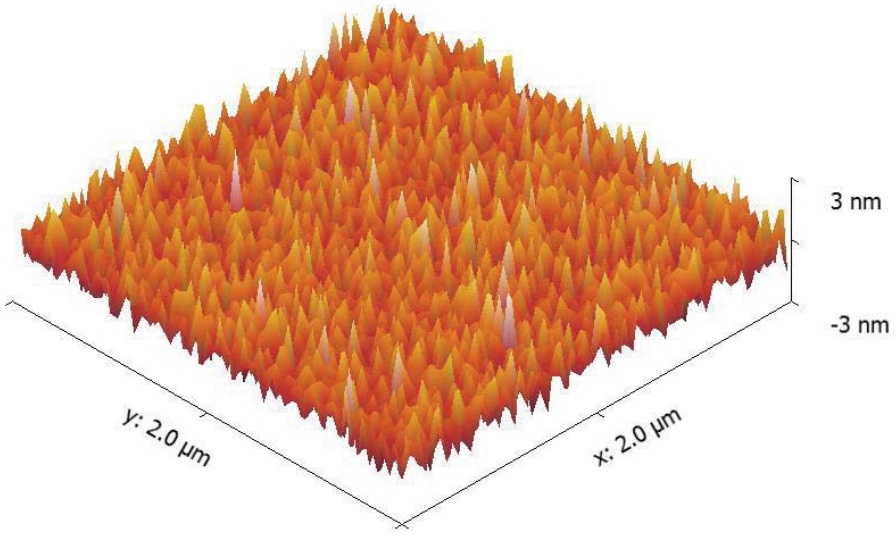

Fig.3. AFM image of the Au surface of the spin valve structure.

2. Scanning Hall Probe Microscopy

Here we introduce the technique of scanning Hall probe microscopy and presents the key experimental conclusions of the measurements made in support of the above manuscript.

2.1 Introduction to the technique

Scanning Hall probe microscopy is a quantitative and non-invasive magnetic imaging technique for measuring the local *perpendicular* component of surface magnetic fields on a sub-micrometer lengthscale. Measurements are based on a cross-shaped Hall effect sensor patterned in the two-dimensional electron gas (2DEG) of an AlGaAs/GaAs heterostructure wafer using electron-beam lithography and wet chemical etching (see Fig.4). After accounting for side wall depletion of carriers we estimate that the width of the active sensor region is 0.6 µm. The large Hall coefficient ($R_H = 1/n_{2D}e \approx 0.3\Omega G^{-1}$) and high mobility of the 2DEG at low temperatures ($\mu \approx 100\ m^2V^{-1}s^{-1}$) make it an excellent material for the fabrication of Hall effect sensors and affords minimum detectable fields of $\sim 2mGHz^{-0.5}$. The Hall probe (HP) is mounted on a piezoelectric scanner tube which allows *fine* nanoscale motion in x-y-z. The piezotube is itself mounted inside a piezoelectric "slip-stick" motor which enables *coarse* motion perpendicular to the sample plane (y-direction). The sensor is

approached towards the sample in coarse steps, after each of which the scanner piezotube fully extends and searches for a tunnel current via an integrated scanning tunnelling tip (STM) that is fabricated ~5 μm from the HP. If no tunnel current is detected the piezotube fully retracts, another coarse approach step is made and the cycle continues until tunnelling is detected. To facilitate the detection of a tunnel current the sample is held at a small voltage bias (~0.2 V), and the tilt angle between sensor and sample is set to ~1-2° to ensure that the STM tip always comes into contact with the surface of the sample first.

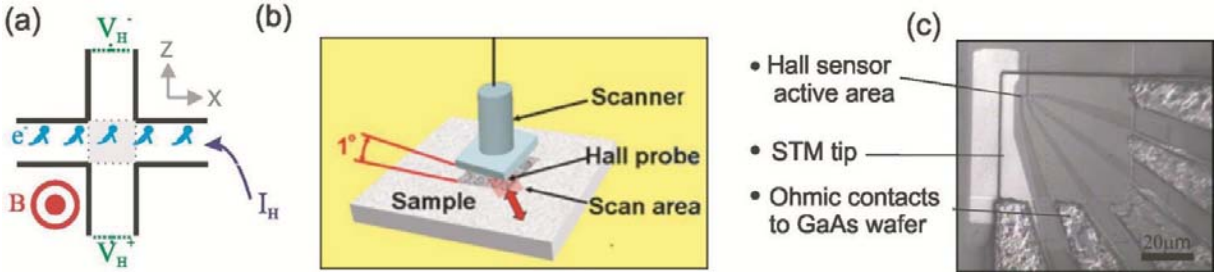

Fig.4. (a) Schematics of the cross-shaped Hall effect sensor and (b) the sample/sensor alignment. (c) An optical micrograph of a sub-micron Hall probe fabricated in an AlGaAs/GaAs heterostructure wafer.

Once tunnel contact is established the sensor is retracted a small distance (~200 nm) from the sample, and scanned at ~0.5 Hz to build up 128 x 128 pixel two-dimensional maps of the local magnetic induction. The temperature dependent scan size is ~57x57 μm^2 at 300 K, ~20x20 μm^2 at 77 K, ~8x8 μm^2 at 4.2 K.

The whole microscope head sits in Helium exchange gas in a commercial variable temperature insert (VTI) of a ^{4}He cryostat which allows control of the temperature between ~300 K and 4.2 K. External in-plane magnetic fields are applied via a room temperature electromagnet that sits on a turntable that allows 360° rotation in the sample plane.

2.2. SHPM measurements of the stray fields at the surface of thin-film spin valve devices

In addition to imaging in constant applied fields, the microscope can also be used to perform static measurements of the local magnetic induction by parking the HP at a fixed location and sweeping the applied field around a hysteresis loop. Fig.5 shows the perpendicular magnetisation measured above a *control sample* when sweeping the in-plane field *collinear* to the pinning direction. This control sample contains only the lower half of the spin valve structure, comprising the IrMn antiferromagnetic pinning layer sandwiched between the two *pinned* ferromagnetic layers: the Co buffer layer underneath and the active pinned F layer on top (see Section 1.1). There is thus no free (unpinned) Co layer or superconducting layer. Comparison with the VSM data of the same sample (see Fig.1) shows that the spikes observed in the 'local' out-of-plane magnetization, M_y, at $\mu_0 H_a \approx -40$ mT and $\mu_0 H_a \approx -50$ mT correspond to the switching of the pinned buffer layer. A sequence of SHPM images taken at the fields indicated in Fig.3a is also presented. Fig.5b illustrates that even at zero applied field, a weak magnetic contrast is visible. Here, darker areas represent regions where flux is directed "down" away from the HP, and lighter areas are where stray fields are pointing "up" out of the sample plane, towards the HP. The perpendicular stray field presumably results from sample inhomogeneities arising from the polycrystalline IrMn antiferromagnetic layer.

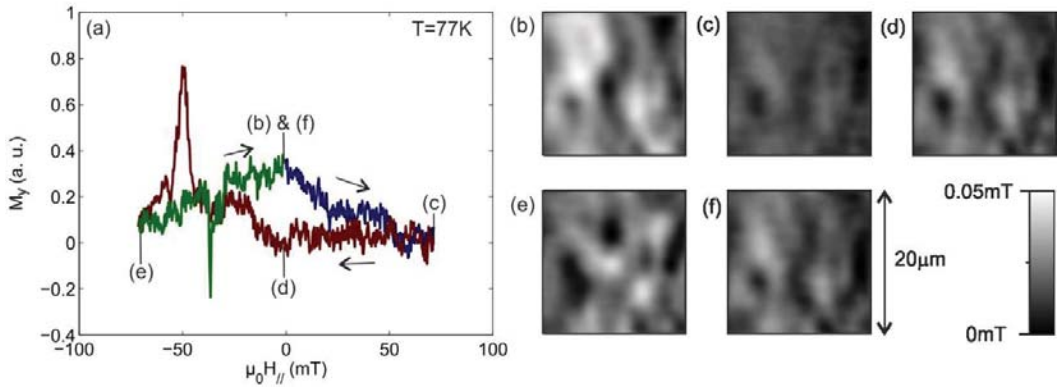

Fig.5. (a) 'Local' magnetisation loop at a fixed position on the control sample at 77 K. (b)-(f) SHPM images at the fields indicated in (a). The applied field is collinear with the exchange biased pinned moment.

The distribution of the stray fields remains approximately constant as the in-plane applied field is swept out to $\mu_0 H_a$=+70 mT and back to zero (3b to 3d). The amplitude of the stray fields drops significantly as the magnetisation becomes more saturated at $\mu_0 H_a$=+70 mT and the moments are increasingly trained in the applied field direction. At $\mu_0 H_a$=-70 mT (3e) the image contrast undergoes a qualitative change when the pinned "buffer" moment reverses direction. Hence *we establish a clear link between contrast in the image and the microscopic magnetisation distribution of the Co layer*. At the end of the loop, the initial field distribution is recovered, indicating that the Co moment has reversed back to its original direction under the exchange bias field.

Fig.6 shows SHPM images of the same control sample with an in-plane field ($\mu_0 H_a$=20 mT), that was originally collinear with the pinned moment (a), and is smoothly rotated out to 90° (c). There is no discernible change to the flux distribution during this rotation and we conclude that *the pinned moments of the control sample are largely unaffected by a rotating in-plane field of this magnitude*.

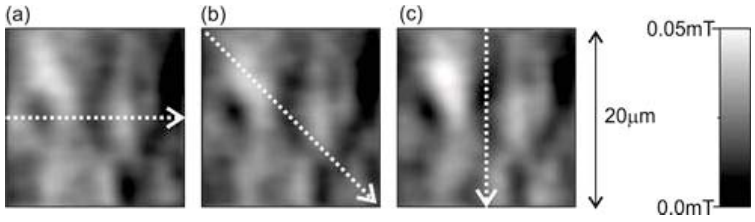

Fig.6. SHPM images of the control sample at T = 77 K, after rotation of a $\mu_0 H_a$=20 mT in-plane field that is (a) initially collinear with, (b) 45° and (c) perpendicular to the exchange biased moment, as indicated by the dashed arrows.

Fig.7 shows the 'local' perpendicular magnetisation, M_y, of the full NSFnF spin valve device during a sweep of a collinear in-plane field while the HP is parked in the centre of the field-of-view. The two sharp and symmetrical switching events observed at $\mu_0 H_a \approx \pm 1.5$ mT correspond to the reversal of the *free* Co layer. SHPM images of the remanent state taken at zero field after saturation in the *antiparallel* (7b) and *parallel* (7c) directions illustrate how the background domain structure reverses contrast when the free layer moment is flipped 180°.

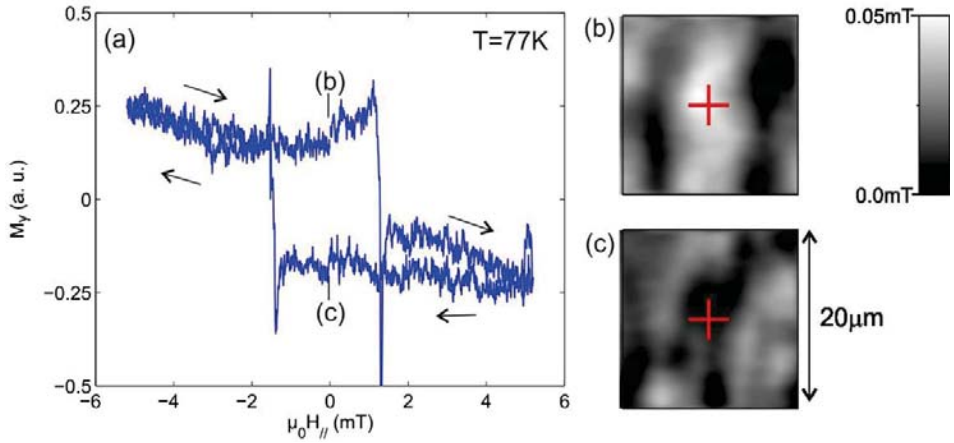

Fig.7. (a) The 'local' perpendicular magnetisation versus in-plane field above a full NSFnF spin valve device. The applied field is collinear with the pinned moment. SHPM images show the remnant magnetisation after saturation in the antiparallel (b) and parallel (c) directions. Crosses in the images indicate the position of the HP during the sweep in (a).

Fig.8 shows SHPM images of the spin valve at 5 K, when the free layer moment is rotated from parallel (θ_{Ha}=0°) to perpendicular (θ_{Ha}=90°) with respect to the pinned moment by an applied in-plane field of $\mu_0 H_a$=10 mT, (8a) and (8b) respectively. The stray field pattern is *independent of the direction of in-plane field* for $T<T_c$ of the S layer. The stray fields at the surface of our samples are therefore very small (<0.5 G) and, at low temperatures ($T<T_c$) these do not change appreciably as the free moment is rotated.

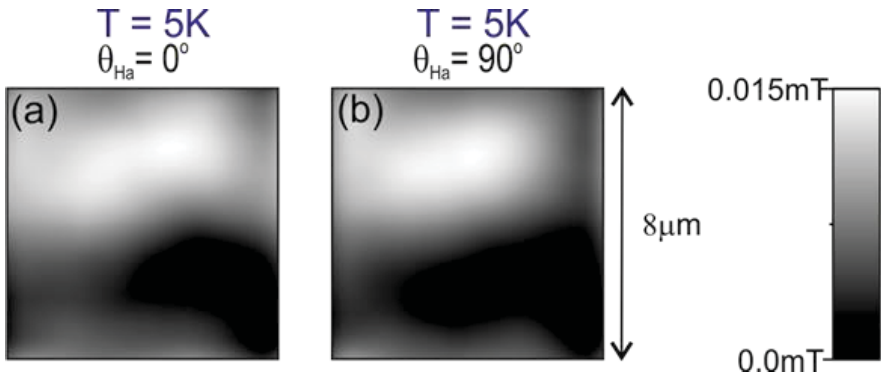

Fig.8. SHPM images of stray fields at the surface of the NSFnF spin valve under rotation of the free Co layer in an applied field of $\mu_0 H_a$=10 mT ($T<T_c$), rotated from parallel with the pinned moment ((a) θ_H=0°) to perpendicular ((b) θ_H=90°).

In conclusion, it is clear that the observed stray fields from both the pinned Co layers and free Co layer are *very small*. Moreover, under the conditions of the experiment, the domain patterns that are observed *do not show any appreciable variation with the in-plane angle* of the applied field. It follows that this is also true for the angle between the pinned and unpinned components of the spin valve. *Any angular dependent variations we observe with the muon experiments can thus not be attributed to changing stray field patterns or domain structures*.

3 Muon Spin Rotation

Here we describe the muon spin rotation technique, the raw data fitting and present additional muon results obtain on our spin valves.

3.1 Measurement technique

In a low energy muon spin rotation (LE-μSR) experiment a single spin polarised muon is implanted into the sample where it rapidly thermalizes typically penetrating to a depth up to ~100 nm (the actual penetration depth of the muon is energy dependent and can be calculated using a well established Monte-Carlo technique). An external field is applied perpendicular to the muon spin polarisation which causes the muon spin to precess at an angular frequency $\omega = \gamma_\mu B$ where γ_μ is the gyromagnetic ratio of the muon and B the local magnetic induction at the muon site. The precession continues until the muon decays (muon lifetime t_μ ~2.2μs) emitting a positron preferentially along the momentary muon spin direction. Positron counter detectors are placed on opposite sides along the sample which allows the time evolution of the muon spin polarisation to be measured after repeating the measurement a high number of times, typically between 1 and 10 million muon decay events are measured.

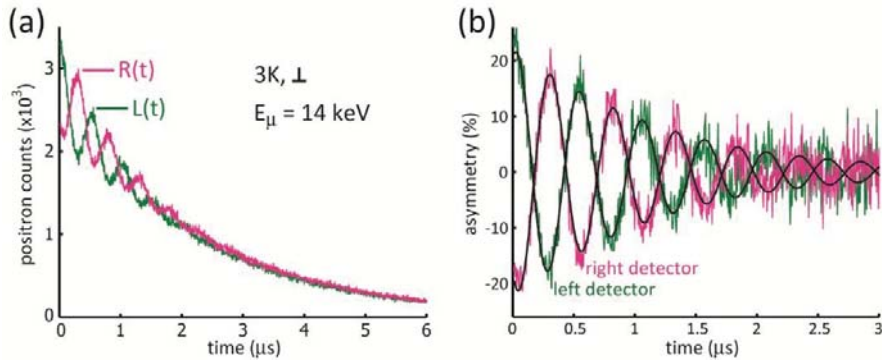

Fig.9 (a) Detector histograms (left (L) and right (R)) from data of Fig.2 of the manuscript taken at T = 3 K and E = 14 keV (corresponding to <y> = 44 nm). (b) Asymmetry of the histograms in (a). The best fit results obtained to both signals are given by black curves.

Fig.9a. shows an example of the detector histograms obtained after taken ~ 3M events. It shows the muon decay process as function of time modulated with a sinusoidal signal due to the muon spin precession. In general the raw data obtained by the left (L) and right (R) positron detectors as a function of time (t) and muon energy (E) can be modelled by: $N_{L/R}(t,E) = N_{0,L/R}(1 \pm A(t,E))\exp(-t/t_\mu) + K_{L/R}$, with N the number of counted positrons, N_0 the amplitude of the signal, K the time-independent background contribution and A(t,E) the asymmetry of the signal which carries all the information concerning the field distributions. It can generally be modelled as $A(t,E)=\int A_0\ p(E,y)\cos(\gamma_\mu B(y)t + \phi(E))G(t,E)dy$, with A_0 the setup-dependent maximum asymmetry that can be measured (for the LEM setup used about 0.23), p(E,y) the muon stopping profile where the depth y is measured normal to the interfaces, B(y) the local flux density, $\phi(E)$ the starting angle of the muon spin precession and G(t,E) the depolarization function ($G \leq 1$) and the integration runs over the full length of the stopping profile. The depolarization function takes into account that B(y) might not be constant along the (x,z)-plane causing the asymmetry to decay over time. Sources that create such inhomogeneities are for example randomly oriented nuclear moments and magnetic strayfields (in the absence of any inhomogeneity G=1). Both sources can be well described by a Lorentzian type of decay $G(t)=\exp(-\lambda t)$ or more generally with a stretched exponential $\exp(-(\lambda t)^\beta)$ (with $1 \leq \beta \leq 2$) to allow for a mixture between Lorentzian and Gaussian type of decay.

3.2 Histogram fitting

A conventional approach to start any muon data analysis is to assume that, as a function of energy, all variables are constant over the depth range of the stopping profile. By fitting the data sets at the measured energies we then obtain the average flux density as function of energy <B>(E). From the muon stopping profiles one can determine the average penetration depth <y> of the muons as function of energy which allows one to convert <B>(E) into <B>(<y>). Ignoring any spatial dependences is clearly incorrect, however, the average flux density obtained does serve as an approximation of the B(y) profile, which is more correct for lower energies (when a thinner slice of the sample is measured). A more correct way of modelling the data is to take all the collected histograms at different energies (but with the sample in an unchanged state) and fit all data simultaneously imposing a single model for B(y) and using the muon stopping profiles to correctly weight each slice of the sample. One can then test different model functions for B(y) and use a chi-square analysis to see which model gives the most consistent fits throughout all the data sets. For our data we used two model functions, a Lorentzian type and a Gaussian type, both with the freedom to either grow or decay over distance inside the Nb. We found that both types give a qualitatively very similar result and both find a best solution for as little induced moment in the Nb as allowed. Fig.10a shows a chi-square analysis of both model functions on the data of Fig.2a of the manuscript (with T = 3 K), where the decay length in the Nb (l_S) is the characteristic decay length over which the model function decays in the Nb. Fig.10b shows the corresponding B(y) profiles for different l_S for the Lorentzian model.

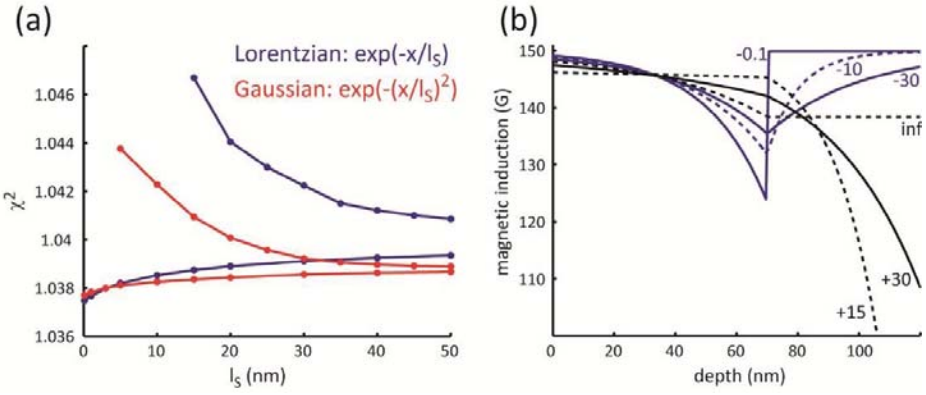

Fig.10. (a) Fits to the data of Fig.2 from the manuscript with T = 3 K for a Lorentzian (blue) and Gaussian (red) type of B(y) profile, with l_S fixed to determine chi-square. The lower branches of each colour are for decaying exponentials in the Nb while the upper branches are for growing exponentials. (b) The corresponding B(y) profiles for the Lorentzian fits for a set of l_S

From this analysis we can thus conclude that the best fits to the T = 3 K data are for a B(y) profile that has as no induced magnetization in the Nb, but does have one at the Au/Nb interface which decays away into the Au over a typical decay length of ~ 20 nm. This absence of any measurable induced magnetization in the superconducting layer is consistent with the results on the thin Au cap sample (Fig.3 in the manuscript) and also with previous LE-μSR measurements on a Py/Nb system[20].

3.3 Induced magnetization for intermediate angles

Measurements were also performed at intermediate angles, one close to collinear arrangement (about 10-15 deg) and one close to orthogonal arrangement (about 75-80 deg). For both only a limited set of points was measured. Data was modelled using the same method as for Fig.2 in the manuscript and the resulting flux profiles are presented in Fig.11. For these measurements the applied field was ~100 G and the base temperature about 2 K higher (compared to the base temperature for the results of Fig.2 in the manuscript) resulting in a smaller induced magnetization. The B(y) of the near orthogonal and near collinear data are of similar magnitude.

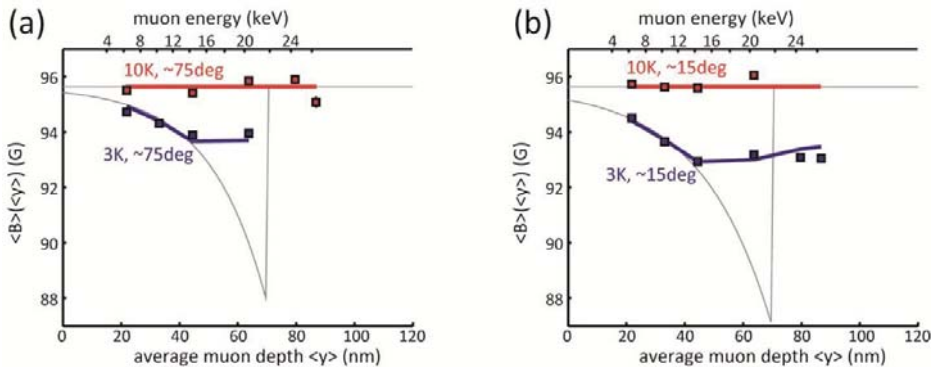

Fig.11. Similar as Fig.2 in the manuscript but now for an angle of (a) about 75-80 deg and (b) about 10-15 deg between the ferromagnet exchange fields. The base temperature was about 2 K higher (still well below T_c) compared to the measurements presented in the manuscript.

4 Theoretical Approaches to the Observed Induced Magnetism

The observed (remote) induced magnetization is not accounted for by current theories. In particular the questions are how the remote magnetization in the normal layer can be provided by the superconductivity of the interlayer, and how this mechanism depends on the mutual orientation of the F layers magnetization, i.e. the spin-valve effect.

4.1 Spin transfer across the superconducting interlayer

Conventional Cooper pairs are in a spin singlet state and as such Andreev reflections at a single interface can't transfer a net spin across the interface. However, since the superconducting correlations extend over the (relatively) large superconducting coherence length scale ξ_S, nonlocal effects (i.e. those using multiple interfaces) such as crossed Andreev reflection (CAR) and elastic co-tunneling (EC)[26] are possible as long as the thickness of the superconductor is of the order of ξ_S. During CAR an electron, say with spin down, originating from the FnF region penetrates through the S/F interface while attracting an electron with opposite spin direction (up) from the N layer, together entering the superconductor creating a Cooper pair. During EC the incoming spin down electron from the FnF region enters the superconductor by pairing with a spin up electron from an already existing Cooper pair, which in turn simultaneously donates its original spin down electron to the N layer. Both processes are sketched in Fig.4 of the manuscript. Here a spontaneous spin accumulation is needed to create an energy-dependent imbalance between the spin density on either side of the superconductor. This imbalance can result from a proximity-induced broken particle-hole symmetry of the spin-resolved density of states in the ferromagnet; for illustrative purpose we replace this situation by an energy region of complete spin-polarization, equivalent to a situation with a spin-dependent chemical potential shift. This imbalance also limits the possible CAR and EC processes.

For CAR a Cooper pair can only be created by taking a spin down electron from the F layer, or annihilated by donating a spin up electron to the F layer. For EC spin down electrons can only move from F to N and spin up electrons can only move from N to F. All possible processes result in a net spin down on the N side and a net spin up on the F side, thus effectively transferring spin across the S layer. However, they also involve charge transfer and in order to maintain charge neutrality (while keeping a net spin transfer) the charge transport for both CAR and EC processes must be cancelled by their reversed processes, i.e. CAR annihilates and creates Cooper pairs at equal rates and EC transfer from N to F and from F to N at equals rates. CAR and EC may thus provide spin transfer through a non-magnetised singlet superconductor over the distance of the coherence length ξ_S. The latter can be estimated as few tens of nanometers for dirty Nb (the thickness of our Nb layer was 50 nm).

The CAR and EC processes essentially describe a net spin current through the superconductor using singlet Cooper pairs, made possible by using nonlocal interfaces. Another possibility would be spin currents based on polarized Cooper pairs, which *do* transfer spin across an interface. Such a triplet spin current is composed of a flow of paired spin-up particles in one direction and an equal in magnitude flow of paired spin-down particles in opposite direction. As pure superconducting spin currents do not transfer or dissipate energy, they do not require a voltage, and they do not require any charge accumulation in the superconductor. However, in order to create nonzero equilibrium superconducting triplet spin-currents through a singlet superconductor there needs to be some form of a broken symmetry. This can happen at interfaces by spin-orbit interaction or in the bulk by dilute magnetic impurities. Dilute magnetic impurities in the S layer may serve twofold: to break particle-hole symmetry, and to break the symmetry between different triplet components due to the spin-orbit interaction.

4.2 The spin-valve effect

The second question to address is the observed spin-valve effect - the disappearance of the remote magnetization together with the long range triplet component (LRTC) at the collinear magnetic

configuration. In which way may the LRTC influence the (nonlocal) transport through the superconductor? In the case of spin currents by spin polarized Cooper pairs the answer is straightforward since the polarized Cooper pairs are created in the FnF region but only for noncollinear magnetization configurations. It is, however, less trivial for these LRTC to lead to a spin transfer across the superconductor where still an additional source of symmetry breaking is required. For the nonlocal CAR and EC processes a different requirement must be met. To transfer the observed negative (opposite to the external magnetic field) remote magnetization into the N layer, some negative spontaneous spin accumulation must exist near the SF interface. It may be ascribed to the inverse proximity effect[14] but that would not depend on the mutual orientation of the F layers magnetization (thus, there would be no spin-valve effect). Spin accumulation appears as a result of spin current decay[28] according to the relation: $n_{\uparrow}$-$n_{\downarrow}$=$\tau^{-1}dj_s/dy$, where $n_{\uparrow}$ and $n_{\downarrow}$ are the concentration of spin-up and -down electrons, respectively, j_s is the spin-current density and τ is the spin-relaxation time.

It was shown that spin currents, both normal[29] and superconducting[30-31], appear in FnF spin-valves with noncollinear spin alignment even in a nonbiased structure, thus providing a mechanism to create the necessary spin accumulation. If the magnetization of the free F layer aligns along the OZ axis and in the pinned F layer along the OX axis (see Fig.1 of the manuscript), then the spin current penetrating from the free F layer into the pinned F layer creates a spin torque, which results in an exchange magnetic interaction between these two F layers. This spin current must have a *y*-spin polarization, other spin projections of the spin current are prohibited by symmetry. Because we detected a negative magnetization along the direction of the applied field (z direction), this indicates the presence of a non-coplanar spin alignment in our structure[30-31]. These may make a contribution to the observed strayfields (see SI Ch.2) attributed to domain structure in our ferromagnetic films. Another possibility may be *y*-spin accumulation appearing at the interface due to decay of the above-mentioned *y*-spin currents. Note that in the collinear geometry the spin currents in the ferromagnetic regions disappear, and so will the remote magnetization. This prediction is consistent with our

observations.